JGR Oceans

RESEARCH ARTICLE
10.1029/2024JC020953

Key Points:

- A new method to identify the Antarctic marginal ice zone is proposed based on statistical clustering of sea ice properties
- Simulated marginal ice zone widths are similar to satellite observations of wave penetration distances
- New understanding gained of differences in ice melt rates and drift speeds between the marginal ice zone and the interior ice pack

Supporting Information:

Supporting Information may be found in the online version of this article.

Correspondence to:

N. S. Day,
noah.day@adelaide.edu.au

Citation:

Day, N. S., Bennetts, L. G., O'Farrell, S. P., Alberello, A., & Montiel, F. (2024). Analysis of the Antarctic marginal ice zone based on unsupervised classification of standalone sea ice model data. *Journal of Geophysical Research: Oceans*, *129*, e2024JC020953. https://doi.org/10.1029/2024JC020953

Received 23 JAN 2024
Accepted 13 AUG 2024

Author Contributions:

Conceptualization: Noah S. Day, Luke G. Bennetts, Siobhan P. O'Farrell, Alberto Alberello, Fabien Montiel
Data curation: Noah S. Day
Formal analysis: Noah S. Day, Luke G. Bennetts
Funding acquisition: Luke G. Bennetts
Investigation: Noah S. Day, Luke G. Bennetts, Siobhan P. O'Farrell, Alberto Alberello
Methodology: Noah S. Day, Luke G. Bennetts, Siobhan P. O'Farrell, Alberto Alberello
Project administration: Luke G. Bennetts
Software: Noah S. Day, Siobhan P. O'Farrell
Supervision: Luke G. Bennetts

Analysis of the Antarctic Marginal Ice Zone Based on Unsupervised Classification of Standalone Sea Ice Model Data

Noah S. Day[1], Luke G. Bennetts[1], Siobhan P. O'Farrell[2], Alberto Alberello[3], and Fabien Montiel[4]

[1]School of Computer and Mathematical Sciences, University of Adelaide, Adelaide, SA, Australia, [2]CSIRO Environment, Aspendale, VIC, Australia, [3]School of Mathematics, University of East Anglia, Norwich, UK, [4]Department of Mathematics and Statistics, University of Otago, Dunedin, New Zealand

Abstract The Antarctic marginal ice zone, the regularly wave-affected outer band of the sea ice covered Southern Ocean, typically contains an unconsolidated ice cover comprised of smaller, thinner floes than the inner ice pack. Thus, it is a highly dynamic region and susceptible to rapid expansion and contraction, making it a focal area for understanding and predicting the response of Antarctic sea ice to a changing climate. This novel study uses unsupervised statistical clustering of sea ice data simulated by a global sea ice model (standalone CICE6 combined with a wave propagation module and prescribed ocean) to address the outstanding challenge of separating the marginal ice zone from the inner ice pack in sea ice data sets. The method identifies a marginal ice zone with the desired characteristics and floe size is shown to be the key variable in the classification. Simulated marginal ice zone widths are similar to those derived from satellite observations of wave penetration distances, but contrast with those using the standard 15%–80% areal sea ice concentration proxy, particularly during austral winter. The simulated marginal ice zone is found to undergo a seasonal transition due to new ice formation in winter, increased drift in spring, and increased rates of wave-induced breakup and melting in summer. The understanding gained from the study motivates incorporation of wave and floe-scale processes in sea ice models, and the methods are available for application to outputs from high-resolution and coupled sea ice–ocean–wave models for more detailed studies of the marginal ice zone (in both hemispheres).

Plain Language Summary The record-setting responses of Antarctic sea ice extent to climate change over recent decades have generated intense research interest in the marginal ice zone at the outskirts of the ice cover. The presence of ocean waves in this region creates a granular ice cover composed of small floes, affecting heat fluxes between the atmosphere and ocean, whilst shielding inner-pack ice, fast ice, and ice shelves from waves. Studies of the marginal ice zone are hindered by the lack of a pragmatic approach to extract the marginal ice zone from sea ice data, which aligns with its characterization as the regularly wave-affected sea ice region. Most studies use a concentration-based proxy, although it overlooks large wave-affected areas. We develop new insights into the evolution of the marginal ice zone by applying a modern machine-learning approach to model outputs, leveraging recent modeling advances. Our findings reveal a marginal ice zone composed of young, small floes during winter and older, fractured floes during summer. Simulated widths are consistent with wave-penetration distance observations and provide evidence of the marginal ice zone's unique properties, including high melt rates. The proposed approach may provide the basis for future studies on its contribution to Antarctic sea ice variability.

1. Introduction

The Antarctic marginal ice zone (MIZ) is the region at the outer margins of the sea ice covered Southern Ocean, where the ice cover is regularly affected by ocean-surface waves, as well as other open-ocean processes (Bennetts et al., 2022b; Wadhams, 1986). Intense atmospheric systems and circumpolar-scale fetches of the Southern Ocean generate large swell waves (Bennetts et al., 2024), creating a considerably larger MIZ than in the Arctic (Weeks, 2010), although MIZ conditions are becoming increasingly common in the Arctic (Stopa et al., 2016; Thomson, 2022). Wave energy attenuates with distance traveled through the MIZ (Meylan et al., 2014; Montiel et al., 2016), so that the MIZ protects the inner ice pack (Squire, 2007), fast ice (Fraser et al., 2023), and ice shelves (Massom et al., 2018; Teder et al., 2022) from waves. Waves regulate the properties of the ice cover in the MIZ, such that the ice floes are relatively small (in size) and are typically unconsolidated (Alberello et al., 2019;

Validation: Noah S. Day, Siobhan P. O'Farrell, Alberto Alberello
Visualization: Noah S. Day, Luke G. Bennetts
Writing – original draft: Noah S. Day, Luke G. Bennetts
Writing – review & editing: Siobhan P. O'Farrell, Alberto Alberello, Fabien Montiel

Toyota et al., 2011, 2016). The nature of the MIZ's ice cover controls heat and momentum fluxes between the atmosphere and ocean (McPhee et al., 1987; Vihma et al., 2014), enhancing sea ice drift (Alberello et al., 2020) and melting (Horvat et al., 2016). Indeed, trends in wave heights and sea ice extents are linked in the Southern Ocean (Kohout et al., 2014), suggesting the rapid expansion and contraction of the MIZ in response to dynamic and thermodynamic forcings (Massom et al., 2008; Vichi et al., 2019) play a role in the long-term variability of Antarctic sea ice extent (J. Turner & Comiso, 2017). Thus, the properties of the MIZ potentially have important implications for the changing state of Antarctic sea ice (Bennetts et al., 2022a; Eayrs et al., 2021). Over the past decade, it has experienced increasing research activity motivated by the responses of both Arctic and Antarctic sea ice to a changing climate (Bennetts et al., 2022b).

Studies that advance understanding of the MIZ and quantify MIZ processes (in both hemispheres) are prohibited by the practical challenge of distinguishing the MIZ from the inner ice pack in sea ice data sets, in a manner consistent with its description as the *regularly* wave-affected region (Squire, 2022). An areal sea ice concentration (SIC) threshold of 15%–80% has been the standard approach to separate the MIZ (10%–80% has also been used by NSIDC, 2023), where the lower and upper limit correspond with thresholds used for sea ice extent (SIE) and "close ice," respectively (Comiso, 2006; WMO, 2014). However, these thresholds have no apparent relation to MIZ dynamics (such as the presence of waves; Dumont, 2022). In particular, during austral winter when the Antarctic SIE is greatest, the outer margins of the ice cover contain large areas near 100% SIC, consisting of pancake ice and interstitial frazil (Alberello et al., 2019; Wadhams et al., 1987), whilst hosting large waves (Alberello et al., 2022).

Over the past decade, the SIC-threshold proxy has been applied to circumpolar satellite data in both hemispheres (Stroeve et al., 2016; Strong, 2012; Strong & Rigor, 2013; Strong et al., 2017) to predict the seasonal cycle of area covered by the MIZ, and has been compared to model data in the Arctic (Rolph et al., 2020). Applying the SIC proxy to satellite products produced an Antarctic MIZ that increases linearly in area from late-austral summer to spring, before peaking in December and returning to a minimum in February (Stroeve et al., 2016; Vichi, 2022). Motivated by observations of Antarctic sea ice drift in regions where the SIC surpasses 80% (Alberello et al., 2020; Womack et al., 2022, 2024), Vichi (2022) recently proposed a method based on the standard deviation of daily SIC anomalies from a monthly-climatological mean (using satellite data) to capture these areas and identify the likelihood of encountering MIZ conditions. Vichi (2022) showed that the SIC-anomaly approach produced a greater rate of growth in Antarctic MIZ area between summer–early-winter, then remained relatively constant until November where it peaked to reach a maximum in December. Soleymani and Scott (2023) studied the seasonal pattern of the Arctic MIZ area using the approach of Vichi (2022).

Studies of MIZ widths have been underpinned by the development of techniques to capture wave height transects within the sea ice cover from ICESat-2 altimetry data in the Antarctic (Brouwer et al., 2022; Horvat et al., 2020), leading to wave-based MIZ approaches (Horvat et al., 2020, who also produced results for the Arctic). Brouwer et al. (2022) applied additional selection criteria to negate uncertainties in wave heights arising from cloud cover, which enabled wave amplitudes smaller than ice freeboard variability to be detected, and resulted in a wider Antarctic MIZ than was found by Horvat et al. (2020). However, both methods produced a maximum MIZ area (and width) during austral winter and a minimum in summer. The seasonality of the wave-defined MIZ area (or width) and significant wave heights in the Southern Ocean (Young et al., 2020) broadly agree (Brouwer et al., 2022), contrasting with results using the SIC-based proxy.

A floe size criterion has been proposed to separate the MIZ from the interior pack ice (Dumont, 2022; Squire, 2022), since the sizes of floes in the MIZ are typically orders of magnitude smaller than floes in the interior pack (Toyota et al., 2011). Application of such an approach to observations is restricted by the scarcity of floe size data, for example, Dumont (2022) applied a floe size criterion to determine the MIZ width over only the southern Fram Strait (Arctic). A floe size-based approach for the MIZ offers the advantage of including regions of the ice-covered ocean that have been affected by waves (e.g., broken floes and pancake ice), even if waves are not present at the particular instant when the data is recorded. Boutin et al. (2022) found agreement between MIZ areas defined by applying a floe-size threshold and a wave-height threshold in Arctic model output were comparable to the wave observations reported by Horvat et al. (2020).

Floe size distributions (FSDs) have recently been implemented into global- and hemispheric-scale sea ice models (e.g., CICE, SI^3/LIM, neXtSIM). The strong relationship between waves and the FSD (Dumont et al., 2011; Mokus & Montiel, 2022; Montiel & Squire, 2017; Williams et al., 2013a, 2013b) motivated the inclusion of wave

impacts within sea ice models (Horvat & Tziperman, 2015; Zhang et al., 2015), and the integration into global sea ice models (Bateson et al., 2020; Bennetts et al., 2017; Boutin et al., 2020; Roach et al., 2019; Roach, Horvat, et al., 2018). Standalone global sea ice models were used to limit computational cost and more easily identify impacts of the FSD on sea ice area and volume. These studies either prescribed the shape of the FSD or used a prognostic FSD (i.e., the shape arises from model physics). Bennetts et al. (2017) and Bateson et al. (2020) both used the waves-in-ice module (Williams et al., 2013a, 2013b) to model floe breakup, and prescribed power laws to the FSD, with simple schemes to represent the welding between floes. Roach, Horvat, et al. (2018) implemented the prognostic joint floe size and ice thickness distribution (FSTD) from Horvat and Tziperman (2015) with the rate of welding determined by the geometric probability that two floes overlap. Roach et al. (2019) furthered this model by letting waves determine the size of new floes (Shen et al., 2001) and coupled CICE to a wave model (WAVEWATCH III). The FSTD is included in CICE6 (Community Ice CodE version 6 Hunke et al., 2017), which is the sea ice component of CESM2 (Community Earth System Model version 2).

In this article, we study the Antarctic MIZ based on a statistical analysis of a decade of daily sea ice model outputs. The statistical analysis utilizes an unsupervised machine learning algorithm (*k*-means clustering) to classify the model data into distinct sea ice regions, and a wave heuristic is used to set the number of clusters. Multiple sea ice variables are included in the statistical analysis, rather than imposing a preferred variable (e.g., SIC or floe size), allowing the algorithm to identify the variables that best separate the sea ice regions. Unsupervised methods have previously been used to separate different sea ice types (e.g., Massom et al., 1999, who used satellite data), and the *k*-means algorithm has been shown to be appropriate for climate science applications (Wilks, 2011) including sea ice data retrieved from satellites (Farooq et al., 2023) and models (such as LIM; Moreno-Chamarro et al., 2020). MIZ widths produced by the exterior *k*-means cluster are compared with those from the standard SIC-threshold proxy, and assessed against satellite observations of wave penetration distances (Brouwer et al., 2022). The statistical clustering approach is used to conduct a study of seasonal physical processes that drive the summer and winter Antarctic MIZ, and to contrast its properties with those of the inner ice pack.

2. Methods

2.1. Numerical Model

2.1.1. Model Configuration

Sea ice model outputs are taken from a modified version of the CICE6 sea ice model (v6.2.0). CICE6 is run in standalone mode with a waves-in-ice module (WIM), which introduces the ocean-surface wave forcing needed to activate FSD routines in CICE6. A CICE6-WIM simulation is conducted from 2005 to 2019 on a tripolar grid with a horizontal resolution of 1° (latitude–longitude), with the first 5 years of simulation treated as spin-up, and, thus, discarded from analysis (Figure S5 in Supporting Information S1). The simulation was forced inter-annually by atmospheric (JRA55-do 1.4.0; Tsujino et al., 2018), oceanic (ACCESS-OM2; Kiss et al., 2020), and ocean-surface-wave model reanalyses (CAWCR Wave Hindcast; Smith et al., 2021). Atmospheric and oceanic data were interpolated to the model timestep (1 hr) from 3-hourly and monthly frequencies, whereas no time interpolation was required to the hourly wave forcing. The wave model reanalysis was forced with surface winds and sea ice from Climate Forecast System Version 2 (Saha et al., 2014). The lower frequency of ocean forcing is due to the slower timescales of sea ice-ocean dynamics compared to sea ice–atmosphere or sea ice–ocean wave interactions (considered by CICE6-WIM).

Standalone CICE6 includes an active mixed-layer ocean calculation, which was forced by atmospheric boundary layer fluxes, sea surface temperature, and salinity (surface current velocities were also input into CICE6-WIM). The CICE6 default restoring time of 90 days and fixed mixed-layer depth of 20 m are used. This simple representation of the mixed-layer ocean leads to an overestimation of sea ice extent compared to satellite observations (Figure S5 in Supporting Information S1; NSIDC, 2023), a known limitation of this approach (Bateson et al., 2020). A simulation of ACCESS-OM2 (a global coupled ocean–sea ice model using MOM5-CICE5; submitted to CMIP6) was used as oceanic forcing (Kiss et al., 2020). For consistency with ACCESS-OM2, CICE6-WIM runs on the same model grid and uses four ice layers with one snow layer to resolve the thermodynamics. The atmospheric forcing is interpolated from a 0.5625° resolution horizontal grid to the model's grid. Initial conditions were adopted from ACCESS-OM2. However, as ACCESS-OM2 used CICE5 with a constant floe size (300 m), the FSD introduced in CICE6, was initialized globally using a fixed power law distribution

(Perovich & Jones, 2014). The smallest category of the FSD contains radii from 0.05 to 2.5 m, allowing for the interpretation of ice types such as frazil, brash, and pancake ice (Roach et al., 2019).

2.1.2. CICE6 Sea Ice Model

CICE6 is a global continuum sea ice model that simulates the evolution of sea ice thickness, h, and floe size (radius), r, as a joint floe size and thickness distribution (FSTD), $f(\mathbf{x}, t; r, h)$, for spatial locations on the ocean surface, $\mathbf{x}$, at times, t. The FSTD is defined such that the areal sea ice concentration within a predefined floe size and thickness category is given by $f(r, h)\,\mathrm{d}r\,\mathrm{d}h$ (Roach, Horvat, et al., 2018), where $\mathrm{d}r$ and $\mathrm{d}h$ are the widths of the respective categories. The FSD is returned by integrating over thickness, the ice thickness distribution (ITD) is returned by integrating over floe size, and the areal sea ice concentration, a_i, is achieved by integrating over both thickness and floe size.

The equation for evolution of the FSTD is (Horvat & Tziperman, 2015)

$$\frac{\partial f(r,h)}{\partial t} = -\nabla\cdot(f(r,h)\mathbf{u}) + \mathcal{L}_T + \mathcal{L}_M + \mathcal{L}_W. \tag{1}$$

The terms on the right-hand side of Equation 1 denote advection, thermodynamics, mechanical deformation processes and wave-induced breakup of sea ice, respectively. Horizontal ice velocity, $\mathbf{u}$, is determined by the output of an elastic-viscous-plastic (EVP) rheological model (Hunke & Dukowicz, 1997). The representative floe size, r_a, is defined by (Roach, Horvat, et al., 2018)

$$r_a = \frac{1}{a_i}\int_{\mathcal{R}}\int_{\mathcal{H}} rf(r,h)\,\mathrm{d}h\,\mathrm{d}r, \tag{2}$$

likewise, the mean ice thickness, h_i, is defined by (Thorndike et al., 1975)

$$h_i = \frac{1}{a_i}\int_{\mathcal{R}}\int_{\mathcal{H}} hf(r,h)\,\mathrm{d}h\,\mathrm{d}r. \tag{3}$$

Thermodynamic processes that affect the FSD are lateral growth and melt, as well as new floe formation and welding of existing floes. Lateral melt is the only floe size process that directly affects all categories of the ITD (Equation S6 in Supporting Information S1), with frazil ice production (resulting in lateral growth or new ice formation) restricted to changes in the thinnest thickness category. As the variable drag option (Tsamados et al., 2014) was not enabled, the FSD does not explicitly appear in the momentum equation (Equations S1 and S2 in Supporting Information S1). Hence, floe radius does not directly affect sea ice dynamics and the FSD is advected as an area-weighted tracer (Equation S3 in Supporting Information S1).

Ocean surface waves directly effect the radius of floes in the FSTD by (a) limiting the size of newly formed floes (promoting the formation of smaller floes, such as pancake ice), or (b) fracturing existing floes via a flexural strain breakup criterion (Horvat & Tziperman, 2015). Given a regular wave (single direction, period and amplitude), the maximum floe size of newly formed floes, $r_{\max}$, is determined by a tensile failure limit (Shen et al., 2001),

$$r_{\max} \approx \sqrt{2\frac{C_2\lambda^2}{\pi^3 A g \rho_i}}, \tag{4}$$

where λ is wavelength, A is wave amplitude, g is gravitational acceleration, ρ_i is ice density, and $C_2 = 0.167\ \mathrm{kg\ m^{-1}\ s^{-2}}$ (Roach, Smith, & Dean, 2018). In irregular sea states, the wavelength is approximated by the representative (peak) wavelength, λ_p, which is calculated using the deep-water surface gravity wave dispersion relation (Williams et al., 2013a),

$$\lambda_p = \frac{2\pi g}{\omega_p^2}, \tag{5}$$

where ω_p is peak-angular frequency (as is used by Roach et al., 2019). By assumption, the amplitude $A = H_s/2$ (Roach, Horvat, et al., 2018), where H_s is significant wave height and is defined by

$$H_s = 4\sqrt{\int S(\omega)\, \mathrm{d}\omega} \tag{6}$$

for a wave spectral density function (SDF), $S(\omega)$, in terms of angular frequency. H_s and ω_p must be input into CICE6 to determine $r_{\max}$ and $\mathcal{L}_W$.

The joint distribution is discretized into a specified number of bins, with default settings allocating five bins for the ITD (Bitz et al., 2001) and 12 bins for the FSD. Consistent with previous studies using the FSTD in CICE, the minimum and maximum floe sizes are set to 0.067 and 850 m, respectively (Bateson et al., 2020; Roach et al., 2019; Roach, Horvat, et al., 2018). An exponential bin spacing scheme is applied to provide finer resolutions for smaller floe sizes. Increasing the number of FSD bins to 16, while offering minimal improvement in agreement with FSD observations, incurs a computational time cost of approximately 60% (Bateson et al., 2020).

2.1.3. Waves-In-Ice Module

The WIM is a modified version of the one developed by Bennetts et al. (2017) for CICE4. The WIM prescribes a frequency–direction SDF one cell north of the 1% SIC edge, where the influence of sea ice on waves is assumed to be negligible. This is achieved by applying an idealized wave-energy spectrum for a given H_s, ω_p, and mean wave direction ($\bar{\theta}$ in radians). These mean wave parameters are taken from a global WAVEWATCH III (WW3) hindcast (Smith et al., 2021).

In this study, assuming a single-peaked directional spectrum, the frequency-directional spectrum, $E(\omega, \theta)$, is given by,

$$E(\omega,\theta) = S(\omega)D\left(\theta - \bar{\theta}\right), \tag{7}$$

where $E(\omega, \theta)$ is the directional SDF, $S(\omega)$ is the frequency SDF, and $D\left(\theta - \bar{\theta}\right)$ is a frequency-independent angular spreading function centered around the mean wave direction. $E(\omega, \theta)$ is integrated over the directional spectrum, such that only southward-waves (due south $\pm\, \pi/2$) enter the sea ice. We set due south to be 0, hence, the incident frequency SDF, $S_{\mathrm{in}}(\omega)$, is initialized by

$$S_{\mathrm{in}}(\omega) = \int_{-\pi/2}^{\pi/2} E(\omega,\theta)\, \mathrm{d}\theta. \tag{8}$$

$S(\omega)$ is initialized using a Bretschneider spectrum (Bretschneider, 1959),

$$S(\omega) = \frac{5}{16} H_s^2 \frac{\omega_p^4}{\omega^5} e^{-\frac{5}{4}\left(\frac{\omega_p}{\omega}\right)^4}, \tag{9}$$

and directional spreading is controlled by a cosine-2s model (Longuet-Higgins, 1963),

$$D\left(\theta - \bar{\theta}\right) = \begin{cases} C\cos^{2s}\left(\dfrac{\theta - \bar{\theta}}{2}\right) & \text{for } \theta - \bar{\theta} \in \left[-\dfrac{\pi}{2}\dfrac{\pi}{2}\right], \\ 0 & \text{otherwise} \end{cases} \tag{10}$$

where C is a normalizing constant. The degree of directional spreading by the cosine-2s function is determined by s. Since the Southern Ocean is dominated by swell, the circular standard deviation of the directional wave energy spectrum, σ_θ, is narrower than wind-driven sea states (Derkani et al., 2021). In accordance with Derkani et al. (2021) who reported that $\sigma_\theta \leq 30°$ when the sea state is dominated by swell, we set $s = 2.5$.

The incident frequency-SDFs, $S_{\text{in}}(\omega)$, are propagated directly southward along meridional lines (i.e., 1D) with frequency-dependent wave attenuation. Wave attenuation is applied cell-wise to the incident SDF by,

$$S_i(\omega) = S_{\text{in}}(\omega)e^{-a_i(x)\alpha(\omega)x} \tag{11}$$

where S_i is the SDF within the ice cover and x is the distance from the ice edge. The attenuation coefficient is determined from an empirical model for Antarctic sea ice, which is scaled by SIC, a_i (Bennetts et al., 2017; Meylan et al., 2014), such that

$$\alpha(\omega) = \frac{1}{a_{i,\text{MBK}}}\left(\beta_2\omega^2 + \beta_4\omega^4\right), \tag{12}$$

where $\beta_2 = 5.38 \times 10^{-5}$, $\beta_4 = 2.95 \times 10^{-5}$ (units of s^2m^{-1} and s^4m^{-1}, respectively), and $a_{i,\text{MBK}} = 0.7$ is the SIC observed in Meylan et al. (2014). CICE6-WIM is forced by the WW3 hindcast and waves are propagated on an hourly basis (matching the model's thermodynamic timestep). Steady-state conditions are assumed for propagation.

This study uses the sea ice physics available in CICE6, such as the FSTD (including its floe breakup model; Horvat & Tziperman, 2015). Unlike Bennetts et al. (2017), we do not prescribe a power-law distribution to the FSD. However, this means that we have uncoupled breakup and wave propagation, that is, no wave energy is lost via wave-induced breakup.

2.2. Data Analysis

2.2.1. Data Overview and Preparation

Five variables are chosen to describe different sea ice types: areal sea ice concentration (a_i), mean ice thickness (h_i), mean snow thickness, representative floe size (r_a), and ice age (see Figure S6 in Supporting Information S1 for the distribution of each variable). Ice age is the average age of the ice within each grid cell and is computed as an ice volume-weighted tracer (see Equation S4 in Supporting Information S1 for its transportation equation). These variables have been used to describe sea ice types in previous studies, for example, unconsolidated pancake or brash ice, young to first-year ice with little snow cover, thicker first-year ice with a thicker snow cover, etc (Massom et al., 1999).

A k-means cluster analysis is performed on daily snapshots of CICE6-WIM model outputs for the five sea ice variables from 2010 to 2019. A 15% SIC mask is used to remove open-ocean cells (similar to Comiso & Zwally, 1984; NSIDC, 2023), so that each cluster can be interpreted as a distinct sea ice type. The data is divided into a specified number, k, of distinct clusters by minimizing the Euclidean distance between each data vector and the cluster centroids (MacQueen, 1967). To complete k-means on data vectors with elements of varying units, the variables must be non-dimensionalized to limit the chance of a single variable dominating the clustering (Wilks, 2011). For example, floe size (which we will now use interchangeably with the representative radius, r_a) has a standard deviation of 300 m, whereas all other variables have standard deviations less than 1 unit. Therefore, we complete min-max scaling on all variables, so that their range is limited between 0 and 1. Since this is a linear transformation, the shapes of the distributions are not affected.

2.2.2. Cluster Number Selection

Figures 1a–1c show daily snapshots from 2019 of the k-means clustered sea ice regions on the day of the mean (over 2010–2019) sea ice extent maximum (26th of August) for $k = 2$–4, respectively. Although the sea ice extent and properties of the ice cover change year to year, the centroids that delineate the clusters remain constant. Regardless of the number of clusters specified to k-means, the clusters produce a pattern of zonal sea ice regions with the southernmost cluster being mostly confined to the Ross and Weddell seas. When $k = 2$, the sea ice is divided into two zonal bands of similar areas. The outer band tends to be the widest east of the Weddell Sea and along the Antarctic Peninsula (~800 km), but narrows in the Ross and Weddell Seas (~400 km). When k is increased from 2 to 3, the exterior cluster for $k = 2$ is split into two regions, with the exterior cluster for $k = 3$ (Cluster 1 in Figure 1) narrower than for $k = 2$ (which is ~100–250 km). The inner part of Cluster 1 for $k = 2$ (i.e.,

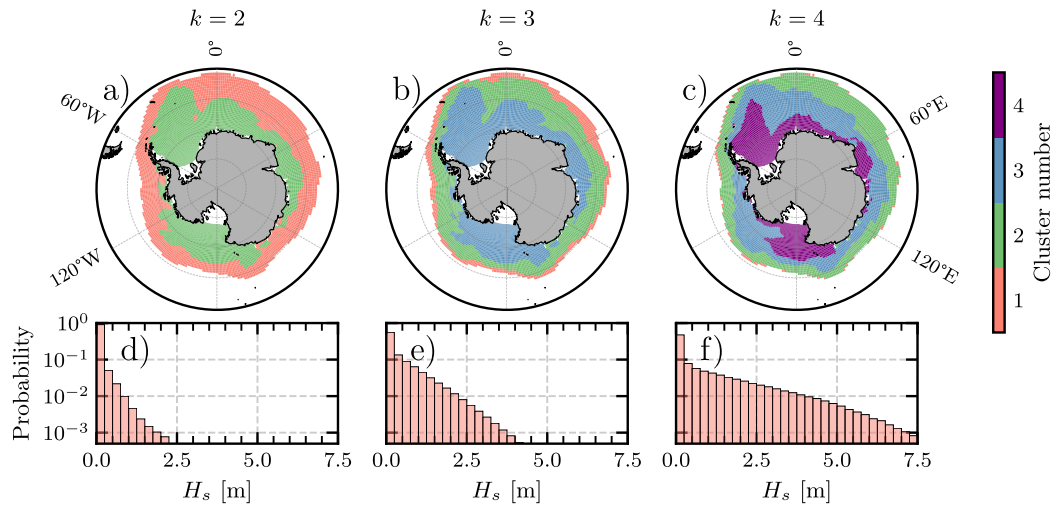

Figure 1. Classification of Antarctic sea ice based on the number of clusters (k) specified to k-means. (a–c) Daily snapshot maps of sea ice clusters on 26 August 2019 (i.e., the average day of the Antarctic sea ice extent maximum over 2010–2019), where (a) $k = 2$, (b) $k = 3$, and (c) $k = 4$. A longitudinal-latitudinal grid (gray dashed lines; in 60° and 10° increments, respectively) is overlaid onto the maps. (d–f) Histograms of significant wave heights (H_s) at the circumpolar southern boundary of Cluster 1 (red) over 2010–2019 on a semi-log scale, for (d) $k = 2$, (e) $k = 3$, and (f) $k = 4$. The sea ice clusters are numbered from lower to higher latitudes.

Cluster 2 for $k = 3$) is an intermediary region between the exterior cluster and the interior ice pack. The addition of a fourth cluster ($k = 4$) predominantly separates the innermost cluster (Cluster 3 for $k = 3$) into two regions, and pushes out the outer two regions (Cluster 1 and Cluster 2 for $k = 3$). Consequently, Cluster 1 for $k = 4$ is typically restricted to only the outermost cell of the ice cover, and no cells for some longitudes.

We determine an appropriate number of clusters for the present study, such that Cluster 1 represents the MIZ, as it agrees (indirectly) with its description as the "actively wave-affected" area of sea ice area of sea ice which is regularly wave-affected (Wadhams, 1986). We interpret this description of the MIZ to be the region where incoming waves from the open ocean remain energetic (H_s order tens of centimeters to meters), with only occasional high-energy waves ($H_s > 1$ m) able to reach (and potentially breakup) the interior sea ice pack (Kohout et al., 2014). We apply a wave-statistic heuristic based on the significant wave height (H_s) at the interior (southern) boundary of the Cluster 1 to quantify the distribution of wave energy transmitted into the interior sea ice pack (i.e., typically the northern boundary of Cluster 2). Histograms of H_s at the interior boundary of Cluster 1 for $k = 2$, 3, and 4 (over 2010–2019) are displayed in Figures 1d–1f, respectively. The mean H_s along this boundary for $k = 2$–4 are 0.08, 0.46, and 1.01 m, respectively. Therefore, we discount $k = 2$, as the waves have become vanishingly small at the southern boundary of its MIZ. The exceedance probability of large waves entering the interior ice pack (i.e., $H_s > 1$ m) is 0.16 for $k = 3$, and 0.35 for $k = 4$. These large waves have a corresponding mean representative wavelength of 250 m for $k = 3$, and 150 m for $k = 4$. Therefore, $k = 3$ is most closely aligned with the requirement for the MIZ to only occasionally allow energetic, long-period waves into the interior pack, hence, three clusters will be used for the rest of the study.

We also applied statistical tests to determine the optimal clusters (standard silhouette and Calinski-Harabasz test Rousseeuw, 1987; Calinski, 1968) for $k = 2$–5, but there was no clear outcome.

3. Results

Results are produced from k-means clustering on 23 million data vectors of scaled CICE6-WIM output variables, with $k = 3$ specified clusters across the sea ice-covered Southern Ocean domain (south of 50°S with $a_i > 15\%$) from 1 January 2010 to 31 December 2019. The labels of the sea ice regions are kept consistent throughout the section and ordered from low to high latitudes, with Cluster 1 denoting the MIZ.

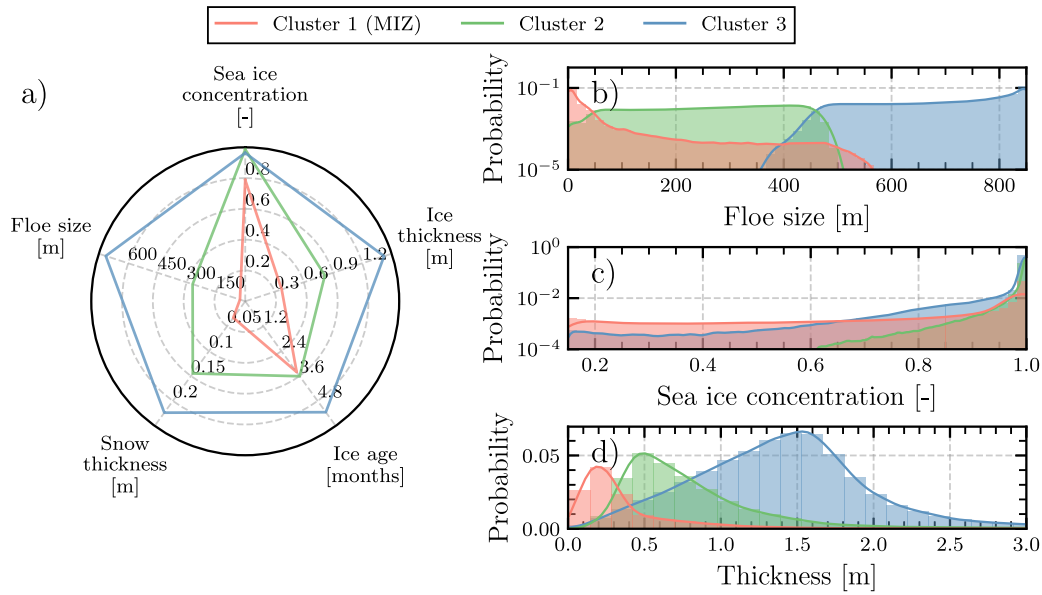

Figure 2. Unscaled centroid locations and distributions of key sea ice variables for Antarctic sea ice clusters. (a) Radar plot of the centroid locations (i.e., the mean sea ice properties) for each cluster. (b–d) Probability density functions grouped by cluster number for three variables: (b) floe size (on a semi-log scale), (c) sea ice concentration (on a semi-log scale), and (d) ice thickness (on a linear scale). The distributions of each variable are normalized, such that the histograms across the three clusters sum to unity.

3.1. Cluster Analysis

Figure 2a shows the unscaled means of each of the sea ice clusters (i.e., back transforming the *k*-means centroids to original units). Floe size, ice and snow thickness are most clearly separated between the clusters and tend to increase with cluster number. Ice age in Cluster 1 and Cluster 2 are similar, indicating that these floes are also mostly belong to the seasonal ice zone (Wadhams, 1986). Sea ice concentrations within Cluster 2 and Cluster 3 are both very high (>95%), with Cluster 1 covering relatively lower concentrations (80%), although 63% of the datapoints in Cluster 1 exceed 80%. The average ice floe within Cluster 1 has a radius of 27 m, is 0.37 m thick and 3.6 months old, with little snow cover (<0.04 m). Cluster 3 generally consists of the largest (>600 m), thickest (>1 m) and oldest (5 months) floes with the most snow cover (>0.2 m). Cluster 2 is an intermediary ice type between the types found in Cluster 1 and Cluster 3, and includes floes of medium size and thickness that found in the highest concentrations (on average) and have a similar age to those in Cluster 1.

Figures 2b–2d show the distributions (histograms with kernel density estimates overlaid) of floe size (semi-log scale), SIC (semi-log scale), and ice thickness (linear scale), respectively. Cluster 1 is characterized by floes smaller than 50 m, with only of 5.6% of floes exceeding 100 m. Cluster 2 is comprised of mostly medium to large floes (100–500 m), and Cluster 3 is dominated by large floes (>550 m). The SIC distributions of all three clusters have a mode greater than 95%, resulting in large overlaps, although the areas of lower concentrations tend to be classified as Cluster 1. Cluster 1 (MIZ) contains the thinnest ice, of which 78.5% is less than 0.5 m thick. The variance of ice thickness in Clusters 2 and 3 are greater than in Cluster 1; both are skewed toward thicker ice, with Cluster 3 containing the majority of ice thicker than 1 m.

3.2. Cluster Identification Dependence on Floe Size

Following the results of Figure 2, a test is completed to determine the influence of floe size on *k*-means clustering. The test includes a comparison of (a) the original data set (as a reference), (b) a data set of only floe size, and (c) a data set of the variables except floe size. Figure 3a shows a daily snapshot (26 August 2019) of the clusters fit to the original data set at the average SIE maximum (as was seen in Figure 1b). The equivalent maps of the new clusters generated from only floe size, and the original data set excluding floe size, are shown in Figures 3b and 3c, respectively (Figure S1 in Supporting Information S1 displays maps at the SIE minimum).

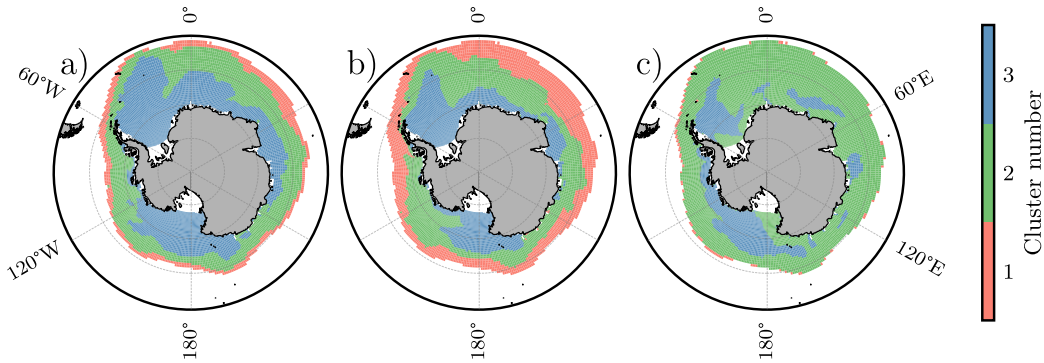

Figure 3. The influence of floe size data on the *k*-means clustering of sea ice. Daily snapshot maps of sea ice clusters on 26 August 2019 are shown for *k*-means clustering using (a) the original data set, (b) only floe size data, and (c) data from all variables except floe size.

All three maps display an outermost cluster (Cluster 1), an innermost cluster (Cluster 3), and an intermediary cluster (Cluster 2). When all variables are used for clustering, the maximum width of Cluster 1 is 253 km and occurs in June. When only floe size data is used (Figure 3b), Cluster 1 widens to a maximum of 520 km (in June) and restricts the two remaining clusters toward the coastline (see Figure S2 in Supporting Information S1 for the separation of floe size amongst the clusters). When floe size is excluded from the clustering (Figure 3c) the maximum width of Cluster 1 during winter is reduced to 17 km (in September) and is restricted to cells along the ice edge. Consequently, Cluster 2 expands, absorbing large portions of the ice cover previously classified as Cluster 1 and Cluster 3. Thus, floe size is the key variable for *k*-means to determine a Cluster 1, which resembles a MIZ (i.e., the wave affected region).

3.3. Evolution of the Antarctic Sea Ice Clusters

Figures 4a–4d show daily snapshot maps of the clusters in four months 2019 (March, June, September, and December, respectively), illustrating their seasonal evolution. Cluster 1 is located along the ocean-sea ice boundary and consistently surrounds the remaining two clusters, typically sharing a boundary with Cluster 2. In March (Figure 4a), the majority of sea ice resides in the Ross and Weddell Seas, and consists of large, thick floes (Cluster 3) with thinner, smaller floes (Cluster 1) skirting the ice edge. During the peak of Antarctic sea ice expansion (April–June; Figure 4b), pockets of Cluster 2 appear along the Antarctic coastline, signifying the formation of new ice (large, thin floes) in coastal polynyas, where waves from CICE6-WIM do not reach. The new ice increases the area of Cluster 2, resulting in it covering the largest fraction of sea ice from May–July. Cluster 3 expands in mid-winter (September; Figure 4c), driven by its increased coverage of the Antarctic coastline, due to the new ice from early winter (i.e., Cluster 2) being reclassified to Cluster 3 as it consolidates and thickens. This culminates in Cluster 3 dominating the ice cover over October–December (Figure 4d).

Figure 4e shows the seasonal areal evolution of each of the clusters (averaged daily over 2010–2019). The area of Cluster 1 reaches two peaks annually, with a maximum in June–July of ∼5 million km^2 and the second peak of ∼3 million km^2 in December. Cluster 2 has an annual maximum area of ∼11 million km^2 (in July) and Cluster 3 has a maximum area of ∼14 million km^2 (in October). As the growth season commences, all three clusters increase in area, with Cluster 2 (i.e., younger, medium–large floes) increasing the most rapidly and becoming dominant in area over winter. The area of Cluster 1 and Cluster 3 grow at similar rates during early winter, although Cluster 1 reaches a maximum area in mid-winter before decreasing over August–September (coinciding with the decrease of Cluster 2). Cluster 3 continues to grow until October (past the date of maximum SIE), before sharply declining in late spring. The rapid loss of area in Cluster 3 occurs during the second growth phase of Cluster 1 in November. Since new ice formation is limited over summer, this suggests that interior sea ice becomes unconsolidated and hence is reclassified as Cluster 1. As a result of this secondary increase, Cluster 1 exhibits the least intraseasonal variability. During the summer, a sharper transition of floe sizes and thickness is formed between the exterior to the interior pack, as Cluster 1 now interfaces with Cluster 3, due to the diminished area of Cluster 2.

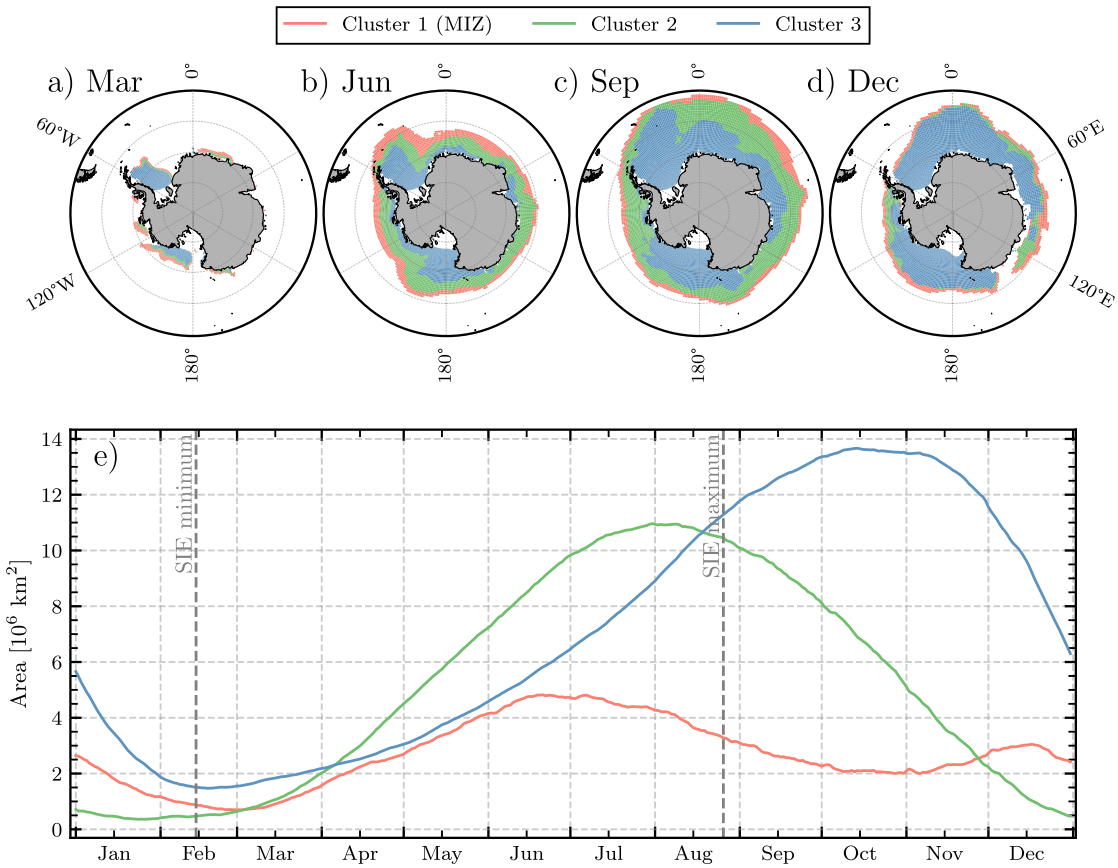

Figure 4. Seasonal spatial and areal evolution of the sea ice clusters. (a–d) Daily snapshots of the sea ice clusters taken on the first of (a) March, (b) June, (c) September, and (d) December 2019. (e) Daily time series of the area within each sea ice cluster, averaged over 2010–2019. The average dates of minimum (14 February) and maximum (26 August) sea ice extent (SIE) shown in dashed gray lines.

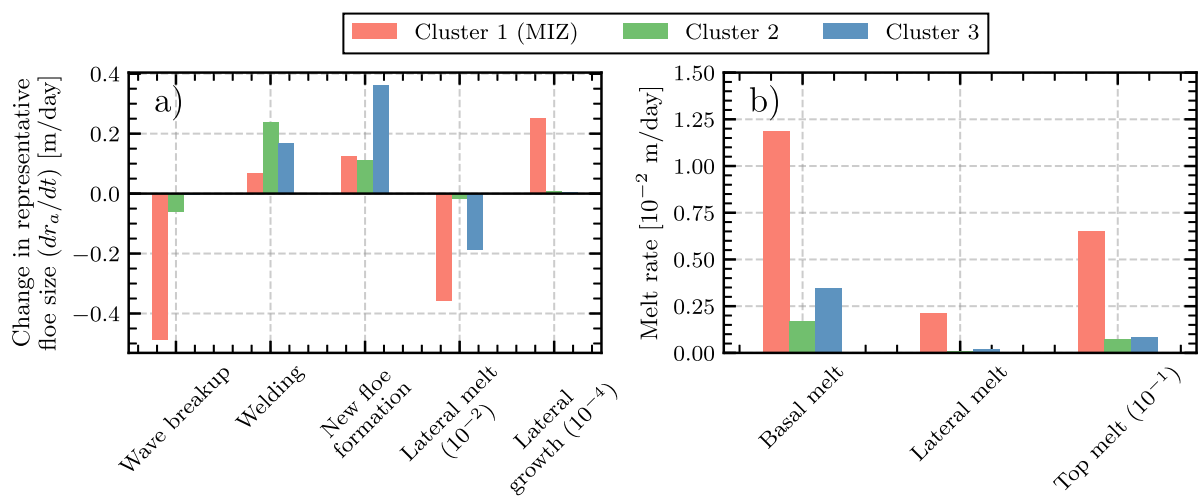

Figure 5. Mean floe size and melt rate tendencies over 2010–2019, grouped by sea ice cluster. (a) Changes in representative floe size per day by each individual processes. (b) Basal, lateral, and top melt rate of sea ice.

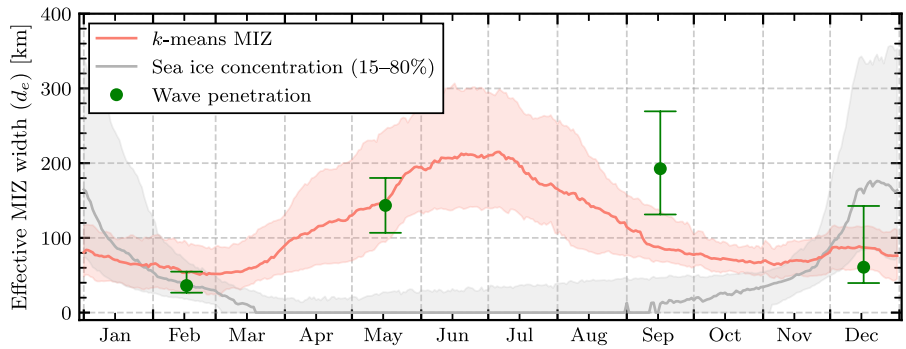

Figure 6. Assessment of MIZ widths from CICE6-WIM outputs compared to satellite observations. Seasonal time series (averaged over 2010–2019) of effective MIZ widths for Cluster 1 from k-means (red) and the 15%–80% sea ice concentration range proxy (gray), shown as daily median values (curves) with interquartile ranges (shaded regions). Monthly medians of satellite-derived wave penetration distances from February, May, September, and December 2019 (Brouwer et al., 2022) are overlaid (green bullets) with their respective interquartile ranges (error bars).

3.4. Floe Size Processes and Melt Rates Across the Antarctic Sea Ice Clusters

Figure 5a shows the average tendencies (over 2010–2019) of the physical processes that affect floe size across the sea ice clusters. The impact on floe size is measured as the change in representative floe size (r_a) per day, where bar heights indicate the mean tendencies and are colored corresponding to cluster number. Wave-induced breakup of floes mainly occurs within Cluster 1 (the MIZ), although Cluster 2 experiences some. Breakup is the dominant process for floe size evolution in Cluster 1, with its mean tendency reducing floe size by 0.49 m day^{-1}. Welding and new floe formation increase floe size by 0.07 and 0.12 m day^{-1}, respectively. New floe formation markedly impacts the representative floe size within Cluster 3, suggesting that new floes generally surpass the size of existing ones. This diagnostic quantifies the change in the FSD imposed by the formation of new ice, rather than the volume of new ice produced. The tendencies of lateral melt and growth change the floe size by -3.59×10^{-3} and 2.5×10^{-5} m day^{-1}, respectively. Welding is the dominant process in Cluster 2, increasing the floe size by 0.24 m day^{-1}. Cluster 3 experiences a similar rate of lateral melt to Cluster 1, as it is the dominant ice cluster over the summer (Figure 4), although, new floe formation is the driver of floe size within Cluster 3.

Figure 5b shows the mean rate of the three modes of sea ice melt (basal, lateral and top) across the sea ice clusters. All three clusters are driven by basal melt, with it being approximately a factor of 10 greater than top melt. Cluster 1 exhibits the greatest melting in all three types, since it is the northernmost cluster and borders the open ocean. Cluster 3 displays the second most melting with Cluster 2 exhibiting the least. As the area of Cluster 2 reduces to less than ∼1 million km^2 over the summer months (Figure 4e), there is only a short period of time for it to experience the increased temperatures, thus, limiting the opportunity for melting.

3.5. Assessment of Antarctic MIZ Widths Against Satellite Observations

To compare with the results of Brouwer et al. (2022), in which effective MIZ widths, d_e, are derived from along-track satellite observations of wave penetration distances into the sea ice cover, the equivalent distance in the direction of propagation (along meridional lines) is calculated by (Wadhams, 1975),

$$d_e = \int_0^d a_i(x)\mathrm{d}x, \tag{13}$$

where d is the distance from the ice edge to the interior MIZ boundary (the southern boundary of Cluster 1), d_e is the width of the ice-covered MIZ along a meridional transect. The effective MIZ width given by the traditional 15%–80% SIC proxy is also shown for reference, that is, the total length of floes in between the 15%- and 80%-SIC contours.

Figure 6 shows the seasonal daily-median effective MIZ widths from k-means (red curve) and the SIC-threshold proxy (gray curve) over 2010–2019, plus their respective interquartile ranges (corresponding shaded areas). The

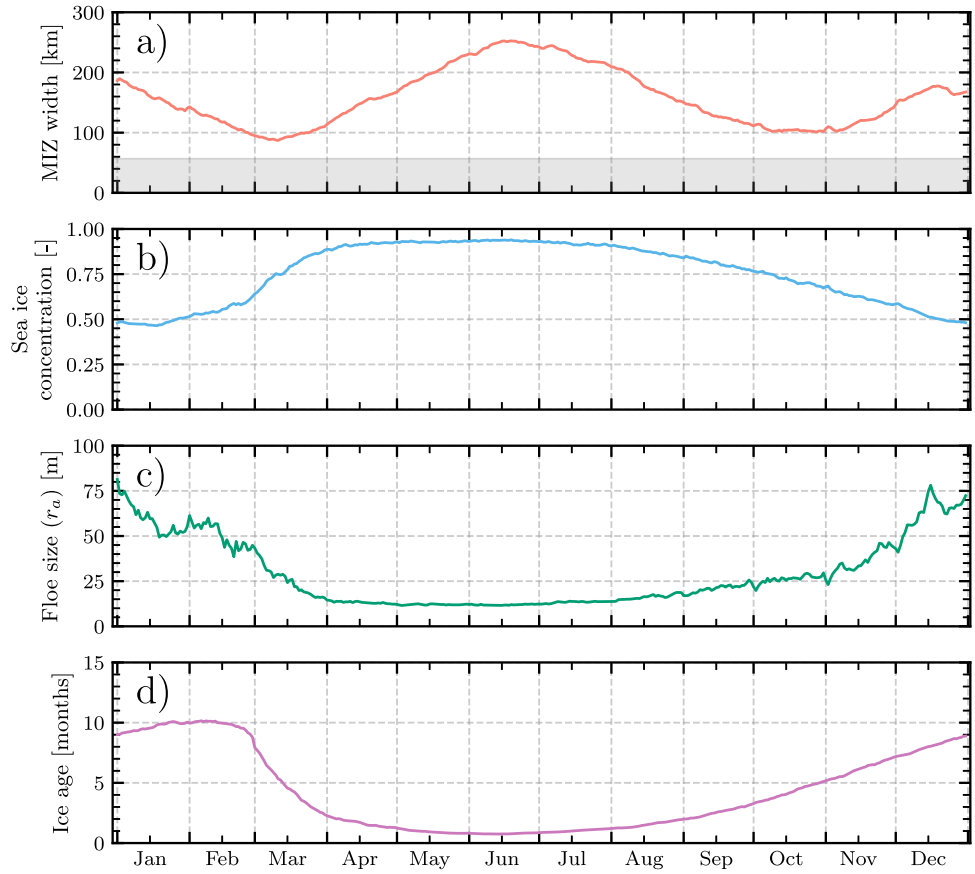

Figure 7. Seasonal time series of Antarctic MIZ (Cluster 1) properties averaged over 2010–2019. Seasonal variations in (a) MIZ width (width of Cluster 1, irrespective of ice concentration), (b) sea ice concentration, (c) representative floe size, and (d) ice age. In panel (a), the average (north–south) width of CICE6-WIM grid cell (∼56 km) is indicated by light gray shading.

effective MIZ width from wave observations by Brouwer et al. (2022) over 2019 are presented as monthly medians and interquartile ranges, for February, May, September and December. As expected, the *k*-means derived effective MIZ width follows the same seasonal shape to the area of Cluster 1 (Figure 4e), with a maximum in July (d_e = 215 km) and a secondary peak in December (d_e = 89 km), although the secondary peak is less pronounced due to reduced sea ice concentrations. The minimum effective MIZ width occurs during the SIE minimum (February; d_e = 51 km). A secondary minimum occurs in spring (6 November), where the MIZ width reduces to d_e = 64 km. In contrast, the SIC-derived effective MIZ width shrinks to a minimum $d_e \approx 0$ km during April–September, when the *k*-means effective MIZ width is greatest, as the SICs at the outer margins of the simulated ice cover often exceeds 80% during winter. The maximum occurs in December (d_e = 176 km), which is twice as wide than that of the *k*-means defined MIZ in summer. When the clustering is completed on the data set excluding floe size, it gives strong agreement with the SIC proxy (see Figure S3 in Supporting Information S1). The effective MIZ width seasonality implied by Brouwer et al. (2022)'s observations is similar to that of the *k*-means MIZ, with a minimum in February (36 km), and a maximum in September (192 km). The *k*-means effective MIZ width strongly agrees with (Brouwer et al., 2022)'s observations in May, and shows good agreement in February and December. Differences are apparent in September, but both have a seasonal maximum of ∼200 km.

3.6. Antarctic MIZ Seasonality

Figure 7a shows the seasonal time series (averaged over 2010–2019) of the absolute MIZ width, d (not to be confused with the effective distance, d_e). For reference, the gray shaded area represents the mean north–south width of a CICE6–WIM grid-cell in the Antarctic domain. The panels below show seasonal time series over

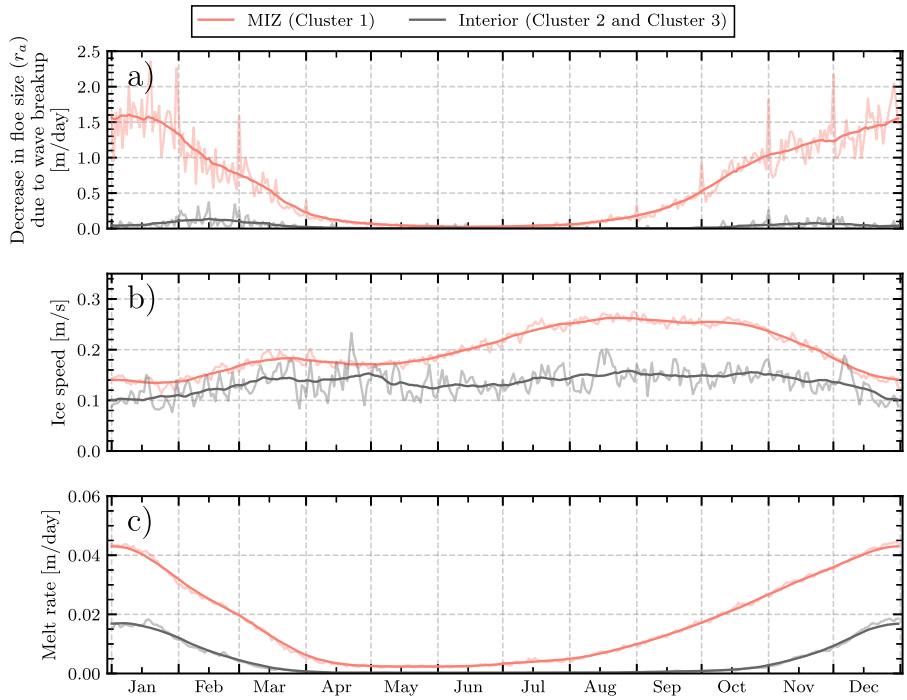

Figure 8. Seasonality of Antarctic sea ice dynamics averaged over 2010–2019. Daily averaged seasonal time series are shown for the MIZ (light red) and interior sea ice (i.e., Clusters 2 and 3 combined in light gray). A 30-day moving average is overlaid for both the MIZ (red) and the interior pack (dark gray). (a) Decrease in floe size from wave-induced breakup, (b) ice speed, and (c) total melt rate.

the same period for the (b) average SIC, (c) representative floe size, and (d) ice age in the MIZ. As expected, the seasonal shape of the mean MIZ width is similar to its mean area (Figure 4e) and median effective MIZ width (Figure 6). It has a maximum of $d = 253$ km in June, and a second peak of $d = 178$ km in December. The summer and spring minima are $d = 87$ km in March and $d = 101$ km in late-October, respectively.

The mean ice age follows a similar seasonal cycle to floe size in the MIZ, with a peak in summer and a low in winter (Figures 7c and 7d). In early winter, the decrease in ice age and floe size simultaneously with the rapid increase in SIC suggests the formation of high-concentration pancake ice fields in the model. Floe sizes reduce to ∼20 m and ice age to less than a month old, which coincides with the annual MIZ width maximum. The spring contraction of the MIZ coincides with a decrease in SIC, and an increase in both floe size and ice age. This transition shifts the floe composition in the MIZ from newly-formed pancakes in high concentrations to lower concentrations of older-larger floes.

Figure 8 shows seasonal (daily-mean) time series of (a) the decrease in representative floe size by wave-induced breakup, (b) sea ice drift speed, and (c) melt rate. The average values within the MIZ (light red) are shown alongside those of the interior sea ice (i.e., Clusters 2 and 3 combined; light gray). A 30-day moving average for both clusters is overlaid (red and dark gray, respectively). The MIZ experiences wave-induced breakup primarily over the summer, and consistently at greater rates than the interior clusters (as expected from Figure 5). Floes in the winter MIZ experience less breakup as their mean representative floe size is limited to ∼20 m (i.e., within the first few categories of the FSD). The moving average of drift speed in the interior remains mostly between 0.1 and 0.15 m s^{-1}. Sea ice drift speeds in the MIZ were also in this range during summer. However, over late-winter to spring the average drift speed within the MIZ increased to approximately 0.1 m s^{-1} greater than that of the interior, coinciding with contraction of MIZ extent (Figure 8a). The rate of melting in the MIZ is greater than the interior pack over the whole annual cycle. As expected, the melt cycle in both the MIZ and interior display strong seasonality with maxima during summer and minima during winter. The MIZ maximum melt rate of 4.35×10^{-2} m day^{-1} is almost triple that of the interior pack (1.49×10^{-2} m day^{-1}). The second MIZ width peak

in December coincides with increased rates of breakup and melting, resulting in the MIZ containing larger broken floes in lower concentrations than in winter.

4. Conclusions and Discussion

Unsupervised classification was used to reduce multivariate daily snapshots of Antarctic sea ice cover properties into statistically defined clusters. The sea ice data set comprised of SIC, ice thickness, ice age, representative floe size, and snow thickness from standalone CICE6-WIM model outputs over 2010–2019. A wave heuristic was used to show that $k = 3$ clusters produced a MIZ-like outer cluster, as the wave-affected region that typically shields the inner ice pack (the two interior clusters) but allows occasional waves to reach the outskirts of the inner pack, for example, large-amplitude waves created by polar storms and cyclones (Kohout et al., 2014; Vichi et al., 2019). The *k*-means cluster analysis identified a MIZ with these properties using only a handful of model variables, which are also easily measurable in the field, compliant with sea ice nomenclature (ASPeCt, 2012).

Floe size emerged as the strongest discriminator of the MIZ, which motivates the development of floe size processes in sea model models, particularly related to ocean wave forcing in the MIZ. However, the role of other variables, such as SIC and ice thickness, were not negligible (as demonstrated by the differences in Figures 3a and 3b, and in Figure S1 in Supporting Information S1), which indicates that descriptions of the MIZ benefit from using more than floe size information alone. The cluster corresponding to the MIZ tended to be comprised of relatively thin floes with little snow cover (Figure 2). During winter, the cluster was found to be comprised of small, young floes in high concentrations, consistent with observations of the winter Antarctic MIZ comprised of pancake ice and interstitial frazil (Alberello et al., 2019; Vichi et al., 2019). In summer, it was composed of larger (relative to winter), older floes in lower concentrations (Figure 7), formed (at least in part) by wave-induced breakup of large, consolidated floes in the inner pack (Figure 8), as observed by Kohout et al. (2016).

Daily outputs of the statistical clustering were used to determine the seasonal behavior of Antarctic MIZ area identified from the model (Figure 4). The area of the MIZ in the standalone model has an annual minimum in mid-summer (1 million km^2) and a maximum in winter (5 million km^2), before it contracts over spring (2 million km^2), and finally reaches a second peak in early-summer (3 million km^2). The winter peak coincides with the expansion of both interior clusters, whereas the summer maximum occurs whilst the area of the interior clusters are decreasing. The average effective MIZ width from the model also displayed this seasonal behavior (although with a reduced summer peak), and was shown to be similar to Brouwer et al. (2022)'s observations based on wave propagation distances, particularly agreeing in February, May, and December (Figure 6). Both methods produced a minimum width of ∼50 km in summer (February), and a maximum width of approximately 200 km in winter. The largest discrepancy occurred in September, which may be a result of the standalone model not capturing the timing of the maximum sea ice extent (e.g., the average date of sea ice extent maximum over 2010–2019 in CICE6-WIM occurred on 26 August, which is over a month prior to the satellite observed maximum on 30 September in 2019; NSIDC, 2023). As sea ice thermodynamics are sensitive to mixed-layer depth (Tsamados et al., 2015), the areal sea ice evolution would likely be improved with a variable depth mixed-layer model, whether coupled to a full-ocean model or a prognostic mixed layer model (Petty et al., 2014).

For the standalone CICE6-WIM model outputs, our statistical clustering approach was shown to produce markedly different MIZ widths to those obtained from the classic 15%–80% SIC proxy (Figure 6). In particular, the SIC-based MIZ widths are at their minimum over the winter months (∼0 km), as the SIC proxy does not identify the MIZ-type driven by the pancake cycle (Lange et al., 1989). This form of the MIZ contains large waves generated by winter cyclones deep into ∼100% concentrations (Alberello et al., 2022), albeit the coarse spatial resolution of the model grid (1° latitude-longitude) prohibits the representation of the steep gradient in SIC between the open ocean and the ice pack (e.g., shown in ASMR2 satellite images; Alberello et al., 2022; Pitt et al., 2022). Thus, the CICE6-WIM outputs underestimate the SIC-defined MIZ (especially when it is less than the average grid-cell length of 56 km). The SIC-defined MIZ sharply increases in width and spread (interquartile range) during summer, which coincides with the *k*-means MIZ increasing in floe size (in mean; Figure 7c) and becoming disperse (mean SIC ∼50%; Figure 7b).

Vichi (2022) found a seasonal MIZ area using the SIC proxy applied to satellite observations that contrasts with our SIC-defined MIZ widths. In particular, he found that the MIZ area grows at a linear rate from 2 million km^2 in February–October, before peaking to 8 million km^2 in December, meaning that it is non-zero over winter (broadly agreeing with the results of Stroeve et al., 2016). The lack of sea ice–ocean feedbacks in our model potentially

exacerbate the amount of frazil ice produced from the thermodynamic scheme (mushy-layer, see A. K. Turner et al., 2013) within CICE (Bailey et al., 2020), which results in increased SICs across the cover and decreases the SIC-threshold MIZ widths during winter. Note that there is previous evidence of significant variability when comparing MIZ areas between satellite products versus model data (Rolph et al., 2020; Stroeve et al., 2016). Further, Vichi (2022) showed that the MIZ area defined by a temporal standard deviation of SIC initially grew at a greater rate than the SIC threshold area (over February–May), and then remained between 5 and 6 million km^2 over winter (similar to the *k*-means winter area; Figure 4). The *k*-means method demonstrates a peak in winter, corresponding to periods of increased sea ice drift. Given that the approach proposed by Vichi (2022) is tailored to pinpoint dynamic areas of the ice pack, it is plausible that similar processes are being captured by his method. Both of the SIC-based approaches Vichi (2022) applied to satellite data identified areas deeper into the pack as MIZ, such as coastal and open-ocean polynyas. These features are not identified as MIZ by the statistical clustering (Figure 3 and Figure S1a in Supporting Information S1), which instead (and by design) returns the outer band of ice cover affected by open-ocean waves (Figures 1 and 8), since no wave generation occurs within the sea ice cover or polynyas in CICE6-WIM.

Floes in the winter Antarctic MIZ have been observed to be highly mobile (e.g., faster drift speeds), and that the wind and ice velocities are strongly correlated (Alberello et al., 2020; Womack et al., 2022, 2024). The CICE6-WIM model results suggest the ice cover in the MIZ and interior pack have comparable speeds during summer (Figure 8c). Throughout the year, speeds in the interior were generally consistent with satellite-derived observations of ice drift (Figure S8; Heil et al., 2006). However, ice speeds in the MIZ increase over July–November, becoming ∼70% greater than in the interior pack. These increased speeds in the MIZ are driven by increased wind stress, The effect of the increased wind stress on modeled sea ice drift in the MIZ is exacerbated by lower internal stresses compared to the interior pack, particularly during August–October when the difference is up to a factor of four (Figure S4b in Supporting Information S1). The modeled internal stress is not directly influenced by floe size (Equation S2 in Supporting Information S1), and the reduced internal stress over spring is more likely due to a reduction in SIC (Figure 7).

Modeled melt rates were found to be greater in the MIZ than in the interior pack, with most of the melting occurring over summer (in both regions). The total melt rate in the MIZ is dominated by basal melt, which is similar to the interior ice pack (Figure 5b). The MIZ experiences greater basal melt than the interior ice pack throughout the year (Figure S7c in Supporting Information S1), by an increased modeled sea surface temperature (calculated by the active mixed-layer; Equation S5 in Supporting Information S1) in the MIZ region. During summer, the basal melt in the MIZ is greater than the interior ice pack by a factor less than two, whereas the total melt is greater by a factor greater than two (Figure S7d in Supporting Information S1). This discrepancy is caused by the contribution of lateral melt to the total melt, and the lateral melt being greater in the MIZ than in the interior pack by a factor of seven (Figure S7b in Supporting Information S1). Smaller floe sizes in the MIZ (relative to the interior) are a key driver of the increased lateral melt (Equation S6 in Supporting Information S1).

In conclusion, understanding of the Antarctic MIZ seasonality has been gained from a standalone sea ice model, both in terms of the area it covers and the properties of the ice cover it contains. The statistical analysis employed identified the Antarctic MIZ in a manner consistent with its description as the regularly wave-affected region of the ice cover (Wadhams, 1986). The inclusion of floe sizes in CICE6-WIM model was essential to identify the MIZ and to study key MIZ processes, such as wave-induced breakup and lateral melt. Future studies should test the proposed methodology on model outputs for Arctic sea ice, in which pancake ice is less prevalent (although suggested to increase with a changing wave climate; Thomson et al., 2017) and the MIZ is generally smaller (Weeks, 2010) as waves rarely penetrate more than 100 km into the MIZ (Cooper et al., 2022). Moreover, studies should be conducted in a coupled model setting, as standalone sea ice models struggle to resolve feedbacks between sea ice and the ocean (including surface waves). Effects on Antarctic MIZ width in response to a more sophisticated wave propagation model that includes additional wave-ice physics should be investigated, for example, where the attenuation rate changes in response to floe size (Meylan et al., 2021) or the inclusion of wave radiation stress on sea ice (Boutin et al., 2021; Dumont, 2022). This will lead to understanding of the influence the MIZ has on the responses of Arctic and Antarctic sea ice covers to the changing climate.

Data Availability Statement

CICE6 is an open source sea ice model and is available at: https://github.com/CICE-Consortium/CICE. The waves-in-ice module (WIM) used for this study along with the output data used to produce this manuscript are available at: https://zenodo.org/records/11081611 (Day et al., 2023). Statistical analysis was completed using Scikit-learn (version 1.1.3, available under the BSD-3-Clause license Pedregosa et al., 2011). The data wrangling and cleaning performed used Xarray (version 2022.11.0, available under the Apache-2.0 license Hoyer & Hamman, 2017) and Pandas (version 1.5.0, available under the BSD-3-Clause license Pandas development team, 2020). Figures were made using Matplotlib (version 3.4.3, license available at https://matplotlib.org/stable/users/project/license.html Hunter, 2007) and maps were created using Cartopy (version 0.20.2, available under the GNU GPLv3 license Met Office, 2010–2015).

Acknowledgments

NSD and LGB are supported by Australian Research Council Grants FT190100404, DP200102828, and LP200100406. NSD is supported by the Consortium for Ocean-Sea Ice Modelling in Australia (COSIMA). AA is supported by the UK EPSRC EP/Y02012X/1. NSD was supported by the Quarterly Journal of Mechanics and Applied Mathematics, DR Stranks Travelling Fellowship, and the Adelaide University Graduate Centre to complete an extended research visit with AA at the University of East Anglia. Model simulations and analysis were completed on the National Computational Infrastructure (NCI), which is supported by the Australian Government. The authors also thank the Isaac Newton Institute for Mathematical Sciences for hosting meetings which conceptualized this study. Open access publishing facilitated by The University of Adelaide, as part of the Wiley - The University of Adelaide agreement via the Council of Australian University Librarians.

References

Alberello, A., Bennetts, L. G., Heil, P., Eayrs, C., Vichi, M., MacHutchon, K., et al. (2020). Drift of pancake ice floes in the winter Antarctic marginal ice zone during polar cyclones. *Journal of Geophysical Research: Oceans*, *125*(3), e2019JC015418. https://doi.org/10.1029/2019jc015418

Alberello, A., Bennetts, L. G., Onorato, M., Vichi, M., MacHutchon, K., Eayrs, C., et al. (2022). Three-dimensional imaging of waves and floes in the marginal ice zone during a cyclone. *Nature Communications*, *13*(1), 4590. https://doi.org/10.1038/s41467-022-32036-2

Alberello, A., Onorato, M., Bennetts, L. G., Vichi, M., Eayrs, C., MacHutchon, K., & Toffoli, A. (2019). Pancake ice floe size distribution during the winter expansion of the Antarctic marginal ice zone. *The Cryosphere*, *13*(1), 41–48. https://doi.org/10.5194/tc-13-41-2019

ASPeCt. (2012). Glossary & image library. Retrieved from https://aspect.antarctica.gov.au/home/glossary-and-image-library.html

Bailey, D. A., Holland, M. M., DuVivier, A. K., Hunke, E. C., & Turner, A. K. (2020). Impact of a new sea ice thermodynamic formulation in the CESM2 sea ice component. *Journal of Advances in Modeling Earth Systems*, *12*(11), e2020MS002154. https://doi.org/10.1029/2020ms002154

Bateson, A. W., Feltham, D. L., Schröder, D., Hosekova, L., Ridley, J. K., & Aksenov, Y. (2020). Impact of sea ice floe size distribution on seasonal fragmentation and melt of Arctic sea ice. *The Cryosphere*, *14*(2), 403–428. https://doi.org/10.5194/tc-14-403-2020

Bennetts, L. G., Bitz, C. M., Feltham, D. L., Kohout, A. L., & Meylan, M. H. (2022a). Marginal ice zone dynamics: Future research perspectives and pathways. *Philosophical Transactions of the Royal Society A*, *380*(2235), 20210267. https://doi.org/10.1098/rsta.2021.0267

Bennetts, L. G., Bitz, C. M., Feltham, D. L., Kohout, A. L., & Meylan, M. H. (2022b). Theory, modelling and observations of marginal ice zone dynamics: Multidisciplinary perspectives and outlooks. *Philosophical Transactions of the Royal Society A*, *380*(2235), 20210265. https://doi.org/10.1098/rsta.2021.0265

Bennetts, L. G., O'Farrell, S., & Uotila, P. (2017). Impacts of ocean-wave-induced breakup of Antarctic sea ice via thermodynamics in a stand-alone version of the CICE sea-ice model. *The Cryosphere*, *11*(3), 1035–1040. https://doi.org/10.5194/tc-11-1035-2017

Bennetts, L. G., Shakespeare, C. J., Vreugdenhil, C. A., Foppert, A., Gayen, B., Meyer, A., et al. (2024). Closing the loops on Southern Ocean dynamics: From the circumpolar current to ice shelves and from bottom mixing to surface waves. *Reviews of Geophysics*, *62*(3), e2022RG00781. https://doi.org/10.1029/2022RG000781

Bitz, C. M., Holland, M. M., Weaver, A. J., & Eby, M. (2001). Simulating the ice-thickness distribution in a coupled climate model. *Journal of Geophysical Research*, *106*(C2), 2441–2463. https://doi.org/10.1029/1999jc000113

Boutin, G., Lique, C., Ardhuin, F., Rousset, C., Talandier, C., Accensi, M., & Girard-Ardhuin, F. (2020). Towards a coupled model to investigate wave–sea ice interactions in the Arctic marginal ice zone. *The Cryosphere*, *14*(2), 709–735. https://doi.org/10.5194/tc-14-709-2020

Boutin, G., Williams, T., Horvat, C., & Brodeau, L. (2022). Modelling the Arctic wave-affected marginal ice zone: A comparison with ICESat-2 observations. *Philosophical Transactions of the Royal Society A*, *380*(2235), 20210262. https://doi.org/10.1098/rsta.2021.0262

Boutin, G., Williams, T., Rampal, P., Olason, E., & Lique, C. (2021). Wave–sea-ice interactions in a brittle rheological framework. *The Cryosphere*, *15*(1), 431–457. https://doi.org/10.5194/tc-15-431-2021

Bretschneider, C. L. (1959). *Wave variability and wave spectra for wind-generated gravity waves* (Vol. 118). The Board.

Brouwer, J., Fraser, A. D., Murphy, D. J., Wongpan, P., Alberello, A., Kohout, A., et al. (2022). Altimetric observation of wave attenuation through the Antarctic marginal ice zone using ICESat-2. *The Cryosphere*, *16*(6), 2325–2353. https://doi.org/10.5194/tc-16-2325-2022

Calinski, T. (1968). A dendrite method for cluster analysis. In *Biometrics* (Vol. 24, p. 207).

Comiso, J. C. (2006). Abrupt decline in the Arctic winter sea ice cover. *Geophysical Research Letters*, *33*(18), L18504. https://doi.org/10.1029/2006gl027341

Comiso, J. C., & Zwally, H. J. (1984). Concentration gradients and growth/decay characteristics of the seasonal sea ice cover. *Journal of Geophysical Research*, *89*(C5), 8081–8103. https://doi.org/10.1029/jc089ic05p08081

Cooper, V. T., Roach, L. A., Thomson, J., Brenner, S. D., Smith, M. M., Meylan, M. H., & Bitz, C. M. (2022). Wind waves in sea ice of the western Arctic and a global coupled wave-ice model. *Philosophical Transactions of the Royal Society A*, *380*(2235), 20210258. https://doi.org/10.1098/rsta.2021.0258

Day, N. S., Bennetts, L. G., O'Farrell, S. P., Alberello, A., & Montiel, F. (2023). Model output: CICE6-WIM Antarctic sea ice data (2010–2019) [Dataset]. *Zenodo*. https://doi.org/10.5281/zenodo.10162320

Derkani, M. H., Alberello, A., Nelli, F., Bennetts, L. G., Hessner, K. G., MacHutchon, K., et al. (2021). Wind, waves, and surface currents in the Southern Ocean: Observations from the Antarctic circumnavigation expedition. *Earth System Science Data*, *13*(3), 1189–1209. https://doi.org/10.5194/essd-13-1189-2021

Dumont, D. (2022). Marginal ice zone dynamics: History, definitions and research perspectives. *Philosophical Transactions of the Royal Society A*, *380*(2235), 20210253. https://doi.org/10.1098/rsta.2021.0253

Dumont, D., Kohout, A. L., & Bertino, L. (2011). A wave-based model for the marginal ice zone including a floe breaking parameterization. *Journal of Geophysical Research*, *116*(C4), C04001. https://doi.org/10.1029/2010jc006682

Eayrs, C., Li, X., Raphael, M. N., & Holland, D. M. (2021). Rapid decline in Antarctic sea ice in recent years hints at future change. *Nature Geoscience*, *14*(7), 460–464. https://doi.org/10.1038/s41561-021-00768-3

Farooq, U., Rack, W., McDonald, A., & Howell, S. (2023). Representation of sea ice regimes in the western Ross Sea, Antarctica, based on satellite imagery and AMPS wind data. *Climate Dynamics*, *60*(1–2), 227–238. https://doi.org/10.1007/s00382-022-06319-9

Fraser, A. D., Wongpan, P., Langhorne, P. J., Klekociuk, A. R., Kusahara, K., Lannuzel, D., et al. (2023). Antarctic landfast sea ice: A review of its physics, biogeochemistry and ecology. *Reviews of Geophysics*, *61*(2), e2022RG000770. https://doi.org/10.1029/2022rg000770

Heil, P., Fowler, C. W., & Lake, S. E. (2006). Antarctic sea-ice velocity as derived from SSM/I imagery. *Annals of Glaciology*, *44*, 361–366. https://doi.org/10.3189/172756406781811682

Horvat, C., Blanchard-Wrigglesworth, E., & Petty, A. A. (2020). Observing waves in sea ice with ICESat-2. *Geophysical Research Letters*, *47*(10), e2020GL087629. https://doi.org/10.1029/2020gl087629

Horvat, C., & Tziperman, E. (2015). A prognostic model of the sea-ice floe size and thickness distribution. *The Cryosphere*, *9*(6), 2119–2134. https://doi.org/10.5194/tc-9-2119-2015

Horvat, C., Tziperman, E., & Campin, J.-M. (2016). Interaction of sea ice floe size, ocean eddies, and sea ice melting. *Geophysical Research Letters*, *43*(15), 8083–8090. https://doi.org/10.1002/2016gl069742

Hoyer, S., & Hamman, J. (2017). xarray: N-D labeled arrays and datasets in Python. [Software]. *Journal of Open Research Software*, *5*(1), 10. In revision. https://doi.org/10.5334/jors.148

Hunke, E. C., & Dukowicz, J. K. (1997). An elastic–viscous–plastic model for sea ice dynamics. *Journal of Physical Oceanography*, *27*(9), 1849–1867. https://doi.org/10.1175/1520-0485(1997)027<1849:aevpmf>2.0.co;2

Hunke, E. C., Lipscomb, W. H., Jones, P., Turner, A. K., Jeffery, N., & Elliott, S. (2017). *CICE, the Los Alamos sea ice model* (Technical Report). Los Alamos National Laboratory (LANL).

Hunter, J. D. (2007). Matplotlib: A 2D graphics environment [Software]. *Computing in Science & Engineering*, *9*(3), 90–95. https://doi.org/10.1109/MCSE.2007.55

Kiss, A. E., Hogg, A. M., Hannah, N., Boeira Dias, F., Brassington, G. B., Chamberlain, M. A., et al. (2020). ACCESS-OM2 v1.0: A global ocean–sea ice model at three resolutions. *Geoscientific Model Development*, *13*(2), 401–442. https://doi.org/10.5194/gmd-13-401-2020

Kohout, A. L., Williams, M. J., Dean, S. M., & Meylan, M. H. (2014). Storm-induced sea-ice breakup and the implications for ice extent. *Nature*, *509*(7502), 604–607. https://doi.org/10.1038/nature13262

Kohout, A. L., Williams, M. J., Toyota, T., Lieser, J., & Hutchings, J. K. (2016). In situ observations of wave-induced sea ice breakup. *Deep Sea Research Part II: Topical Studies in Oceanography*, *131*, 22–27. https://doi.org/10.1016/j.dsr2.2015.06.010

Lange, M. A., Ackley, S. F., Wadhams, P., Dieckmann, G. S., & Eicken, H. (1989). Development of sea ice in the Weddell Sea. *Annals of Glaciology*, *12*, 92–96. https://doi.org/10.3189/s0260305500007023

Longuet-Higgins, M. S. (1963). The effect of non-linearities on statistical distributions in the theory of sea waves. *Journal of Fluid Mechanics*, *17*(3), 459–480. https://doi.org/10.1017/s0022112063001452

MacQueen, J. (1967). Some methods for classification and analysis of multivariate observations. In *Proceedings of the 5h Berkeley symposium on mathematical statistics and probability* (Vol. 1, pp. 281–297).

Massom, R. A., Comiso, J. C., Worby, A. P., Lytle, V. I., & Stock, L. V. (1999). Regional classes of sea ice cover in the East Antarctic pack observed from satellite and in situ data during a winter time period. *Remote Sensing of Environment*, *68*(1), 61–76. https://doi.org/10.1016/s0034-4257(98)00100-x

Massom, R. A., Scambos, T. A., Bennetts, L. G., Reid, P., Squire, V. A., & Stammerjohn, S. E. (2018). Antarctic ice shelf disintegration triggered by sea ice loss and ocean swell. *Nature*, *558*(7710), 383–389. https://doi.org/10.1038/s41586-018-0212-1

Massom, R. A., Stammerjohn, S. E., Lefebvre, W., Harangozo, S. A., Adams, N., Scambos, T. A., et al. (2008). West Antarctic Peninsula sea ice in 2005: Extreme ice compaction and ice edge retreat due to strong anomaly with respect to climate. *Journal of Geophysical Research*, *113*(C2), C02S20. https://doi.org/10.1029/2007jc004239

McPhee, M. G., Maykut, G. A., & Morison, J. H. (1987). Dynamics and thermodynamics of the ice/upper ocean system in the marginal ice zone of the Greenland Sea. *Journal of Geophysical Research*, *92*(C7), 7017–7031. https://doi.org/10.1029/jc092ic07p07017

Met Office. (2010–2015). Cartopy: A cartographic python library with a Matplotlib interface [Software]. *Exeter, Devon*. Retrieved from https://scitools.org.uk/cartopy

Meylan, M. H., Bennetts, L. G., & Kohout, A. L. (2014). In situ measurements and analysis of ocean waves in the Antarctic marginal ice zone. *Geophysical Research Letters*, *41*(14), 5046–5051. https://doi.org/10.1002/2014gl060809

Meylan, M. H., Horvat, C., Bitz, C. M., & Bennetts, L. G. (2021). A floe size dependent scattering model in two-and three-dimensions for wave attenuation by ice floes. *Ocean Modelling*, *161*, 101779. https://doi.org/10.1016/j.ocemod.2021.101779

Mokus, N. G., & Montiel, F. (2022). Wave-triggered breakup in the marginal ice zone generates lognormal floe size distributions: A simulation study. *The Cryosphere*, *16*(10), 4447–4472. https://doi.org/10.5194/tc-16-4447-2022

Montiel, F., & Squire, V. A. (2017). Modelling wave-induced sea ice break-up in the marginal ice zone. *Proceedings of the Royal Society A: Mathematical, Physical and Engineering Sciences*, *473*(2206), 20170258. https://doi.org/10.1098/rspa.2017.0258

Montiel, F., Squire, V. A., & Bennetts, L. G. (2016). Attenuation and directional spreading of ocean wave spectra in the marginal ice zone. *Journal of Fluid Mechanics*, *790*, 492–522. https://doi.org/10.1017/jfm.2016.21

Moreno-Chamarro, E., Ortega, P., & Massonnet, F. (2020). Impact of the ice thickness distribution discretization on the sea ice concentration variability in the NEMO3.6–LIM3 global ocean–sea ice model. *Geoscientific Model Development*, *13*(10), 4773–4787. https://doi.org/10.5194/gmd-13-4773-2020

NSIDC. (2023). Sea ice index daily and monthly image viewer. Retrieved from https://nsidc.org/data/seaice_index

Pandas development team. (2020). pandas-dev/pandas: Pandas [Software]. *Zenodo*. https://doi.org/10.5281/zenodo.3509134

Pedregosa, F., Varoquaux, G., Gramfort, A., Michel, V., Thirion, B., Grisel, O., et al. (2011). Scikit-learn: Machine learning in Python [Software]. *Journal of Machine Learning Research*, *12*, 2825–2830. https://www.jmlr.org/papers/volume12/pedregosa11a/pedregosa11a.pdf

Perovich, D. K., & Jones, K. F. (2014). The seasonal evolution of sea ice floe size distribution. *Journal of Geophysical Research: Oceans*, *119*(12), 8767–8777. https://doi.org/10.1002/2014jc010136

Petty, A. A., Holland, P. R., & Feltham, D. L. (2014). Sea ice and the ocean mixed layer over the Antarctic shelf seas. *The Cryosphere*, *8*(2), 761–783. https://doi.org/10.5194/tc-8-761-2014

Pitt, J. P., Bennetts, L. G., Meylan, M. H., Massom, R. A., & Toffoli, A. (2022). Model predictions of wave overwash extent into the marginal ice zone. *Journal of Geophysical Research: Oceans*, *127*(10), e2022JC018707. https://doi.org/10.1029/2022jc018707

Roach, L. A., Bitz, C. M., Horvat, C., & Dean, S. M. (2019). Advances in modeling interactions between sea ice and ocean surface waves. *Journal of Advances in Modeling Earth Systems*, *11*(12), 4167–4181. https://doi.org/10.1029/2019ms001836

Roach, L. A., Horvat, C., Dean, S. M., & Bitz, C. M. (2018). An emergent sea ice floe size distribution in a global coupled ocean-sea ice model. *Journal of Geophysical Research: Oceans*, *123*(6), 4322–4337. https://doi.org/10.1029/2017jc013692

Roach, L. A., Smith, M. M., & Dean, S. M. (2018). Quantifying growth of pancake sea ice floes using images from drifting buoys. *Journal of Geophysical Research: Oceans*, *123*(4), 2851–2866. https://doi.org/10.1002/2017jc013693

Rolph, R. J., Feltham, D. L., & Schröder, D. (2020). Changes of the Arctic marginal ice zone during the satellite era. *The Cryosphere*, *14*(6), 1971–1984. https://doi.org/10.5194/tc-14-1971-2020

Rousseeuw, P. J. (1987). Silhouettes: A graphical aid to the interpretation and validation of cluster analysis. *Journal of Computational and Applied Mathematics*, *20*, 53–65. https://doi.org/10.1016/0377-0427(87)90125-7

Saha, S., Moorthi, S., Wu, X., Wang, J., Nadiga, S., Tripp, P., et al. (2014). The NCEP climate forecast system version 2. *Journal of Climate*, *27*(6), 2185–2208. https://doi.org/10.1175/jcli-d-12-00823.1

Shen, H. H., Ackley, S. F., & Hopkins, M. A. (2001). A conceptual model for pancake-ice formation in a wave field. *Annals of Glaciology*, *33*, 361–367. https://doi.org/10.3189/172756401781818239

Smith, G. A., Hemer, M., Greenslade, D., Trenham, C., Zieger, S., & Durrant, T. (2021). Global wave hindcast with Australian and Pacific island focus: From past to present. *Geoscience Data Journal*, *8*(1), 24–33. https://doi.org/10.1002/gdj3.104

Soleymani, A., & Scott, A. (2023). Arctic marginal ice zone interannual variability and change point detection using two definitions (1983–2022). *Environmental Research Letters*, *18*(12), 124002. https://doi.org/10.1088/1748-9326/ad0609

Squire, V. A. (2007). Of ocean waves and sea-ice revisited. *Cold Regions Science and Technology*, *49*(2), 110–133. https://doi.org/10.1016/j.coldregions.2007.04.007

Squire, V. A. (2022). A prognosticative synopsis of contemporary marginal ice zone research. *Philosophical Transactions of the Royal Society A*, *380*(2235), 20220094. https://doi.org/10.1098/rsta.2022.0094

Stopa, J. E., Ardhuin, F., & Girard-Ardhuin, F. (2016). Wave climate in the Arctic 1992–2014: Seasonality and trends. *The Cryosphere*, *10*(4), 1605–1629. https://doi.org/10.5194/tc-10-1605-2016

Stroeve, J. C., Jenouvrier, S., Campbell, G. G., Barbraud, C., & Delord, K. (2016). Mapping and assessing variability in the Antarctic marginal ice zone, pack ice and coastal polynyas in two sea ice algorithms with implications on breeding success of snow petrels. *The Cryosphere*, *10*(4), 1823–1843. https://doi.org/10.5194/tc-10-1823-2016

Strong, C. (2012). Atmospheric influence on Arctic marginal ice zone position and width in the Atlantic sector, February–April 1979–2010. *Climate Dynamics*, *39*(12), 3091–3102. https://doi.org/10.1007/s00382-012-1356-6

Strong, C., Foster, D., Cherkaev, E., Eisenman, I., & Golden, K. M. (2017). On the definition of marginal ice zone width. *Journal of Atmospheric and Oceanic Technology*, *34*(7), 1565–1584. https://doi.org/10.1175/jtech-d-16-0171.1

Strong, C., & Rigor, I. G. (2013). Arctic marginal ice zone trending wider in summer and narrower in winter. *Geophysical Research Letters*, *40*(18), 4864–4868. https://doi.org/10.1002/grl.50928

Teder, N. J., Bennetts, L. G., Reid, P. A., & Massom, R. A. (2022). Sea ice-free corridors for large swell to reach Antarctic ice shelves. *Environmental Research Letters*, *17*(4), 045026. https://doi.org/10.1088/1748-9326/ac5edd

Thomson, J. (2022). Wave propagation in the marginal ice zone: Connections and feedback mechanisms within the air–ice–ocean system. *Philosophical Transactions of the Royal Society A*, *380*(2235), 20210251. https://doi.org/10.1098/rsta.2021.0251

Thomson, J., Ackley, S., Shen, H. H., & Rogers, W. E. (2017). The balance of ice, waves, and winds in the Arctic autumn. *Eos*, *98*. https://doi.org/10.1029/2017eo066029

Thorndike, A. S., Rothrock, D. A., Maykut, G. A., & Colony, R. (1975). The thickness distribution of sea ice. *Journal of Geophysical Research*, *80*(33), 4501–4513. https://doi.org/10.1029/jc080i033p04501

Toyota, T., Haas, C., & Tamura, T. (2011). Size distribution and shape properties of relatively small sea-ice floes in the Antarctic marginal ice zone in late winter. *Deep Sea Research Part II: Topical Studies in Oceanography*, *58*(9–10), 1182–1193. https://doi.org/10.1016/j.dsr2.2010.10.034

Toyota, T., Kohout, A., & Fraser, A. D. (2016). Formation processes of sea ice floe size distribution in the interior pack and its relationship to the marginal ice zone off East Antarctica. *Deep Sea Research Part II: Topical Studies in Oceanography*, *131*, 28–40. https://doi.org/10.1016/j.dsr2.2015.10.003

Tsamados, M., Feltham, D. L., Petty, A., Schröder, D., & Flocco, D. (2015). Processes controlling surface, bottom and lateral melt of Arctic sea ice in a state of the art sea ice model. *Philosophical Transactions of the Royal Society A*, *373*(2052), 20140167. https://doi.org/10.1098/rsta.2014.0167

Tsamados, M., Feltham, D. L., Schröeder, D., Flocco, D., Farrell, S. L., Kurtz, N., et al. (2014). Impact of variable atmospheric and oceanic form drag on simulations of Arctic sea ice. *Journal of Physical Oceanography*, *44*(5), 1329–1353. https://doi.org/10.1175/jpo-d-13-0215.1

Tsujino, H., Urakawa, S., Nakano, H., Small, R. J., Kim, W. M., Yeager, S. G., et al. (2018). JRA-55 based surface dataset for driving ocean–sea-ice models (JRA55-do). *Ocean Modelling*, *130*, 79–139. https://doi.org/10.1016/j.ocemod.2018.07.002

Turner, A. K., Hunke, E. C., & Bitz, C. M. (2013). Two modes of sea-ice gravity drainage: A parameterization for large-scale modeling. *Journal of Geophysical Research: Oceans*, *118*(5), 2279–2294. https://doi.org/10.1002/jgrc.20171

Turner, J., & Comiso, J. C. (2017). Solve Antarctica's sea-ice puzzle. *Nature*, *547*(7663), 275–277. https://doi.org/10.1038/547275a

Vichi, M. (2022). An indicator of sea ice variability for the Antarctic marginal ice zone. *The Cryosphere*, *16*(10), 4087–4106. https://doi.org/10.5194/tc-16-4087-2022

Vichi, M., Eayrs, C., Alberello, A., Bekker, A., Bennetts, L. G., Holland, D. M., et al. (2019). Effects of an explosive polar cyclone crossing the Antarctic marginal ice zone. *Geophysical Research Letters*, *46*(11), 5948–5958. https://doi.org/10.1029/2019gl082457

Vihma, T., Pirazzini, R., Fer, I., Renfrew, I. A., Sedlar, J., Tjernström, M., et al. (2014). Advances in understanding and parameterization of small-scale physical processes in the marine Arctic climate system: A review. *Atmospheric Chemistry and Physics*, *14*(17), 9403–9450. https://doi.org/10.5194/acp-14-9403-2014

Wadhams, P. (1975). Airborne laser profiling of swell in an open ice field. *Journal of Geophysical Research*, *80*(33), 4520–4528. https://doi.org/10.1029/jc080i033p04520

Wadhams, P. (1986). The seasonal ice zone. In *The geophysics of sea ice* (pp. 825–991). Springer.

Wadhams, P., Lange, M. A., & Ackley, S. F. (1987). The ice thickness distribution across the Atlantic sector of the Antarctic Ocean in midwinter. *Journal of Geophysical Research*, *92*(C13), 14535–14552. https://doi.org/10.1029/jc092ic13p14535

Weeks, W. (2010). *On sea ice*. University of Alaska Press.

Wilks, D. S. (2011). *Statistical methods in the atmospheric sciences* (Vol. 100). Academic Press.

Williams, T. D., Bennetts, L. G., Squire, V. A., Dumont, D., & Bertino, L. (2013a). Wave–ice interactions in the marginal ice zone. Part 1: Theoretical foundations. *Ocean Modelling*, *71*, 81–91. https://doi.org/10.1016/j.ocemod.2013.05.010

Williams, T. D., Bennetts, L. G., Squire, V. A., Dumont, D., & Bertino, L. (2013b). Wave–ice interactions in the marginal ice zone. Part 2: Numerical implementation and sensitivity studies along 1D transects of the ocean surface. *Ocean Modelling*, *71*, 92–101. https://doi.org/10.1016/j.ocemod.2013.05.011

WMO. (2014). Sea-ice nomenclature. Retrieved from https://library.wmo.int/idurl/4/41953

Womack, A., Alberello, A., de Vos, M., Toffoli, A., Verrinder, R., & Vichi, M. (2024). A contrast in sea ice drift and deformation between winter and spring of 2019 in the Antarctic marginal ice zone. *The Cryosphere*, *18*(1), 205–229. https://doi.org/10.5194/tc-18-205-2024

Womack, A., Vichi, M., Alberello, A., & Toffoli, A. (2022). Atmospheric drivers of a winter-to-spring Lagrangian sea-ice drift in the Eastern Antarctic marginal ice zone. *Journal of Glaciology*, *68*(271), 999–1013.

Young, I. R., Fontaine, E., Liu, Q., & Babanin, A. V. (2020). The wave climate of the Southern Ocean. *Journal of Physical Oceanography*, *50*(5), 1417–1433. https://doi.org/10.1175/jpo-d-20-0031.1

Zhang, J., Schweiger, A., Steele, M., & Stern, H. (2015). Sea ice floe size distribution in the marginal ice zone: Theory and numerical experiments. *Journal of Geophysical Research: Oceans*, *120*(5), 3484–3498. https://doi.org/10.1002/2015jc010770

References From the Supporting Information

Hibler, III, W. D. (1979). A dynamic thermodynamic sea ice model. *Journal of Physical Oceanography*, *9*(4), 815–846. https://doi.org/10.1175/1520-0485(1979)009<0815:adtsim>2.0.co;2

Hunke, E. C., & Bitz, C. M. (2009). Age characteristics in a multidecadal Arctic sea ice simulation. *Journal of Geophysical Research*, *114*(C8), C08013. https://doi.org/10.1029/2008jc005186

Josberger, E. G., & Martin, S. (1981). A laboratory and theoretical study of the boundary layer adjacent to a vertical melting ice wall in salt water. *Journal of Fluid Mechanics*, *111*, 439–473. https://doi.org/10.1017/s0022112081002450

Maykut, G. A., & McPhee, M. G. (1995). Solar heating of the Arctic mixed layer. *Journal of Geophysical Research*, *100*(C12), 24691–24703. https://doi.org/10.1029/95jc02554

Maykut, G. A., & Perovich, D. K. (1987). The role of shortwave radiation in the summer decay of a sea ice cover. *Journal of Geophysical Research*, *92*(C7), 7032–7044. https://doi.org/10.1029/jc092ic07p07032

Rothrock, D. A. (1975). The energetics of the plastic deformation of pack ice by ridging. *Journal of Geophysical Research*, *80*(33), 4514–4519. https://doi.org/10.1029/jc080i033p04514

Rothrock, D. A., & Thorndike, A. S. (1984). Measuring the sea ice floe size distribution. *Journal of Geophysical Research*, *89*(C4), 6477–6486. https://doi.org/10.1029/jc089ic04p06477

Schröder, D., Feltham, D. L., Tsamados, M., Ridout, A., & Tilling, R. (2019). New insight from CryoSat-2 sea ice thickness for sea ice modelling. *The Cryosphere*, *13*(1), 125–139. https://doi.org/10.5194/tc-13-125-2019

Steele, M. (1992). Sea ice melting and floe geometry in a simple ice-ocean model. *Journal of Geophysical Research*, *97*(C11), 17729–17738. https://doi.org/10.1029/92jc01755